Int. J. Electrochem. Sci., 12 **(2017)** 4585 – 4596, doi: 10.20964/2017.05.78

International Journal of
ELECTROCHEMICAL
SCIENCE
www.electrochemsci.org

A Mesoporous Structure SnP_2O_7/Graphite Oxide Composite as Proton Conducting Electrolyte for High-Temperature Proton Exchange Membrane Fuel Cells

Min Huang[1], *Xin Huang*[1], *MingMing Fei*[1,2], *Yuming Deng*[1,2], *Xiaozhou Huang*[1], *Chenxi Xu*[1,*], *Jigui Cheng*[1,*], *Paifeng Luo*[1], *Yinwei Lu*[1]

[1] School of Materials Science and Engineering, Hefei University of Technology, Hefei, Anhui, China
[2] Institute of industry & Equipment technology, Hefei University of Technology, Hefei, Anhui, China
[*]E-mail: xuchenxi31@126.com, jgcheng63@sina.com

Received: 25 January 2017 / *Accepted:* 16 March 2017 / *Published:* 12 April 2017

Proton conductors operated in over 200°C have received great interest for proton exchange membrane fuel cells (PEMFCs). The tetravalent metal ion pyrophosphates materials (MP_2O_7) are considered as the suitable conductor electrolyte, and the mesopores structure MP_2O_7 are attractive, because capillary condensation of water molecules occurs at relatively low relative humidity, allowing for fast transport of protons without excessive humidification. In this study, we report meso-SnP_2O_7, which is synthesized from mesoporous SnO_2, as promising solid electrolyte candidate for PEMFCs in a temperatures range of 180°C to 280°C. Furthermore, graphite oxide (GO) is incorporated with the meso-SnP_2O_7 to further improve the proton conductivity and water retention. The structure and phase stability of the membranes are analysed by X-ray diffraction (XRD) and thermos-gravimetric analysis (TGA). The microstructure morphology of SnP_2O_7 particles and pellets is analysed by transmission electron microscope (TEM) and scanning electron microscopy (SEM). The obtained particles and pores size of Meso-SnP_2O_7 are characterized by the ETA potential meter and BET. The Meso-SnP_2O_7 and Meso-SnP_2O_7/GO electrolytes exhibit the high proton conductivities of 0.15 S cm^{-1} and 0.17 S cm^{-1} at 220°C, respectively. Moreover, the peak power densitiy of the Meso-SnP_2O_7/GO membrane is 18 $mWcm^{-2}$ at 220 °C with OCV of 0.83V.

Keywords: High-temperature proton exchange membrane fuel cells; Graphite Oxide; mesoporous structure; capillary condensation

1. INTRODUCTION

Operating proton exchange membrane fuel cells (PEMFCs) at elevated temperatures (≥200°C) could enhance the electrode reaction kinetics, which allow for low Pt loading or even the use of a non-

noble catalyst. Furthermore, a high tolerance to CO of catalyst could simplify the fuel pre-treatment techniques. On the other hand, operating a fuel cell under low RH obviates the need for a complicated humidity control system [1-4]. The proton membranes that can bear temperatures over 200°C for PEMFC are usually made of inorganic materials, Recently, a number of tetravalent metal pyrophosphates (MP_2O_7 , where M = Sn, Ge,Zr, Si, Ce, Ti) have shown proton conductivity [5-8]. Park et al. researched CeP_2O_7, which exhibited a conductivity of 2.1×10^{-4} S cm^{-1} at 175°C [9]. Hibino et al. [7.8] reported that the proton conductivities of SnP_2O_7 materials have conductivity via doping with trivalent elements. However, the low conductivity and weak strengths of MP_2O_7 membranes limit their application to high-temperature PEMFCs.

The mesoporous inorganic materials have a large internal surface area leading to a capillary condensation of water molecules that occurs at relatively low relative humidity (RH), which leads to easy transport of protons without excessive humidification [10]. As porous framework materials, mesoporous structures have many ordered or disordered nano-size channels. Therefore, the mesoporous structure could improve their water adsorption capacity and proton conductivity under high temperature. The proton conductor such as P_2O_5 could dissolve in water and presence in these pores. These pyrophosphates in themselves are proton conducting materials, there may be synergy between the framework and mesopores spaces [11].

The modify filler used in inorganic materials could also improve the conductivity and strengthen membranes. As our previous work reported [12], GO with different acidic functional groups provides more proton hopping, and also it extends the number of available ion exchange sites per cluster, resulting in increased proton mobility [12-14]. Therefore, GO could be a suitable doping to improve composite membrane proton conductivities at high temperatures. pyrophosphates could be considered as suitable electrolyte candidate for HTPEMFC. The conductivity and fuel cell performance of mesoporous structure SnP_2O_7 electrolyte are further improved with the incorporation of GO.

2. EXPERIMENTAL

Mesoporous SnO_2 powders were synthesized as follow. 5g Sodium dodecyl sulfate (SDS) was dissolved in 100 mL deionized water, and 2.5g $Na_2SnO_3{\cdot}3H_2O$ was added to the solution with stirring at room temperature. After 60 min of stirring, the pH was adjusted gradually to ca. 10, 8, 6, 4, and 2 with 36% hydrochloric acid solution for every 60 min interval. The solution gradually became a white suspension when the pH decreased. The solid product was filtered and rinsed with ethanol, and also dried under vacuum oven at room temperature for 1 day. The SDS surfactant was removed by stirring the specimen adding an ammonia–water and ethanol mixture for 1 day. After filtering, washing, and drying, the SnO_2 powder was obtained. Mesoporous SnP_2O_7 powders were obtained from the mesoporous SnO_2 powder mixed with a phosphoric acid solution at a molar ratio of P/Sn=2,and 5 wt% GO was mixed with the mesoporous SnP_2O_7. The composite membrane is mesoporous SnP_2O_7/GO .The mixture was stirred at 110 °C until the viscosity paste achieved. The paste was heated in an alumina crucible to 550 °C at a rate of 5 °C min^{-1}. Finally, the compound was ground with a

mortar and pestle. A nonporous SnP_2O_7 powder was also prepared through a commercially available SnO_2. The compound powder was uniaxially pressed into pellets (13 mm diameter) a pressure of 200 MPa for 5 min and then sintered at 250 °C for 8 hrs in air. For conductivity measurements, the pellet was painted with colloidal silver on both sides, and dried in an oven at 120°C for about 2 hrs until colloidal silver was solidified. A silver wire mesh connected to a silver wire was separately placed in contact with the painted pellet on both sides and was pressed against mica sheets to ensure proper electrical contact. The proton conductivity was measured with Autolab PGSTAT302. The impedance measurements were carried out between frequencies of 1 and 10 kHz. The perturbation voltage was kept at 10mV. The crystal structures of different powders were analysed using X-ray diffraction (XRD,X'Pert PROMPD), with a scan range of 5–70°. The morphologies of the SnP_2O_7 membranes were investigated via a SU-8020 Scanning Electron Microscope (SEM). The thermal behaviour was analysed by thermos-gravimetric analysis (TGA, STA449F3). The pore volume and pore size distributions were calculated using the Barrett–Joyner–Halenda (BJH) method.

In this study, a mesoporous structure SnP_2O_7 was synthesized from mesoporous SnO_2. Structural, physicochemical, and electrical analyses of the obtained products were carried out in this work. The membrane proton conductivities and the fuel cell performances over 200°C were characterised, and these results indicate that the mesoporous structure tetravalent metal ion Brunauer–Emmett–Teller (BET) specific surface areas were measured through nitrogen adsorption using a conventional flow-type adsorption apparatus. The particle size were characterized at 25°C for 1 min by ETA potential meter (Nano-ZS90, Malvern)The catalyst ink (40 wt% Pt/C in a water–ethanol mixture) was directly deposited on the membranes for both the anode and cathode, and the MEAs were held at a temperature of 150 °C [2]. The Pt loading was 0.1 mg cm^{-2}. Two gas chambers were arranged by placing a galvanic cell between two alumina tubes and sealing with an inorganic adhesive; the temperature was controlled by a heating furnace. The silver wires were connected to the samples by a conductive adhesive. 5 vol% H_2/Ar and air were fed into the anode and cathode at flow rates of 100 cm^3 min^{-1} and at atmospheric pressure, respectively.

3. RESULTS AND DISCUSSION

The crystalline structures of a mesoporous and nonporous SnO_2 were characterized by XRD analysis in Fig. 1. The diffraction patterns of the mesoporous SnO_2 corresponded to a tetragonal rutile structure and the peaks were much broader than those of the nonporous SnO_2 because of a much smaller crystallite size [11]. The XRD structural also confirms that the diffraction peaks at 19.43° 23.48°, 26.70°, 27.57°, 31.95°, 33.97°, 39.36° and 45.90° belong to the (111), (210), (210), (211), (221), (311), (230) and (400) crystal planes of nonporous SnP_2O_7 (JCPDS 00-029-1352) [16]. The mesoporous SnP_2O_7 exhibited the single cubic phase structure after 500ºC treating. In addition, the mean particle size of mesoporous SnP_2O_7 estimated as 180.6 nm according the Scherrer formula, was smaller than that of nonporous SnP_2O_7 （385.9 nm）which is also agreed by the result from laser particle size analyzer [11, 16]. GO diffraction peak at 2θ=9.42° corresponding to the (001) plane reflection, which is left in comparison to the typical peak of 10.5° reported in our previous work [12]

indicating that the mesoporous SnP_2O_7 particles are inserted and expand the GO exfoliation layer distance.

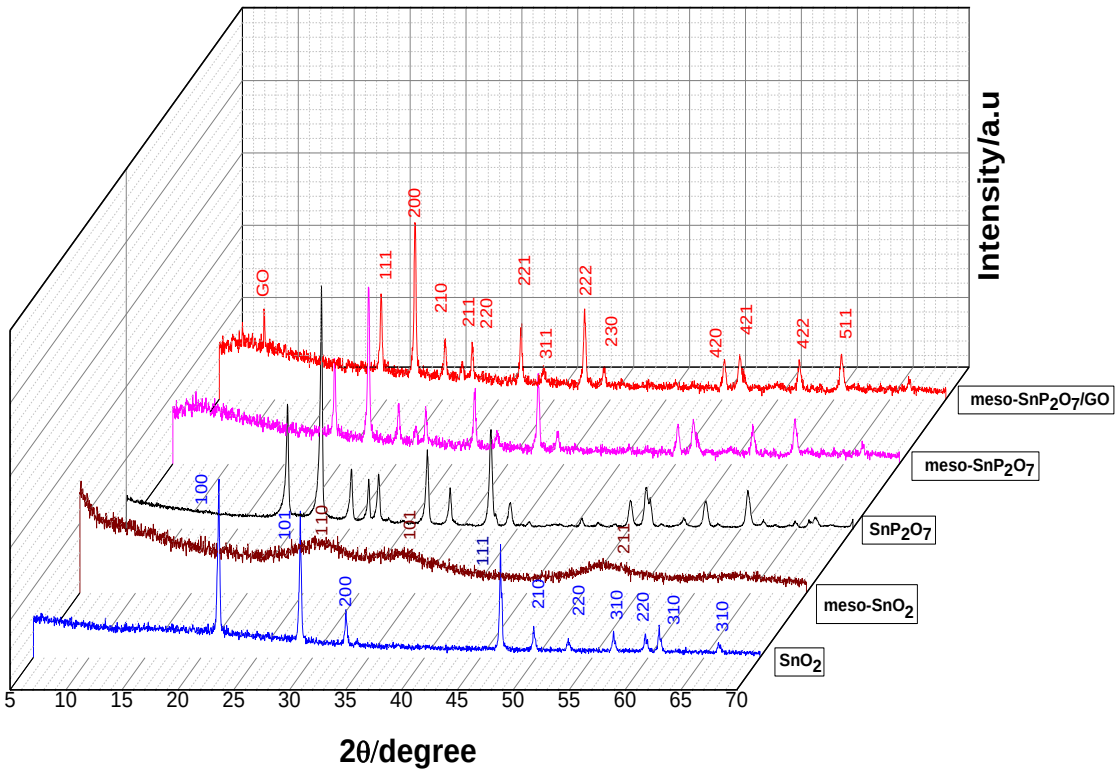

Figure 1. XRD spectra of SnP_2O_7, Meso-SnP_2O_7 and Meso-SnP_2O_7/GO

Figure 2 depicts the non-porous and mesoporous SnP_2O_7 particle size distribution by ETA potential meter. The particle sizes of meso-SnP_2O_7 are ranged from 100 nm to 600nm contrasting to the sizes between 250nm to 950 nm of the non-porous SnP_2O_7. The average particle diameter of non-porous SnP_2O_7 is 458.7 nm, which is nearly twice as large as that of mesoporous SnP_2O_7 (255 nm). These results are similar to the values calculated from Scherrer formula. However, both the two kinds particles are over hundred nanometres because the particles size grows up when temperature increasing during the sintering. The smaller particle size benefits to achieve a narrow pore size and even the mesoporous state.

The non-porous and mesostructure of SnP_2O_7 was observed using TEM. Fig. 3 exhibits that square and hexagonal structures exist in the mesoporous SnP_2O_7, which is different morphology from the structure of the nonporous SnP_2O_7. The mesoporous SnP_2O_7 structure appears the observed square and hexagonal arrangement is distorted and disordered, which is conformed to the XRD results. The diameter of meso-SnP_2O_7 is around hundred nanometres from TEM, and this result is similar to the ETA predicts values.

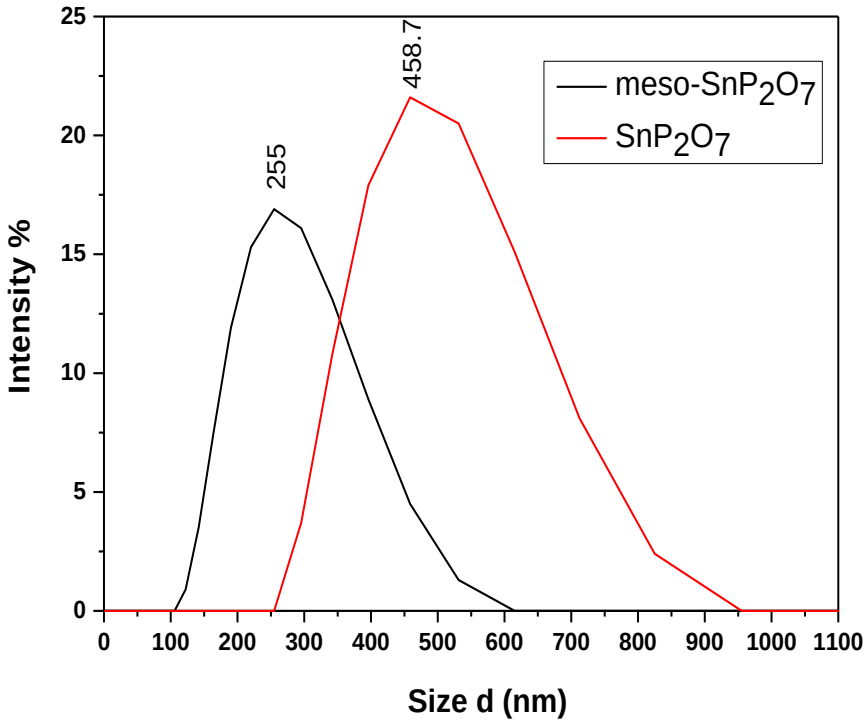

Figure 2. The Particles size distribution of the mseo-SnP_2O_7 and SnP_2O_7

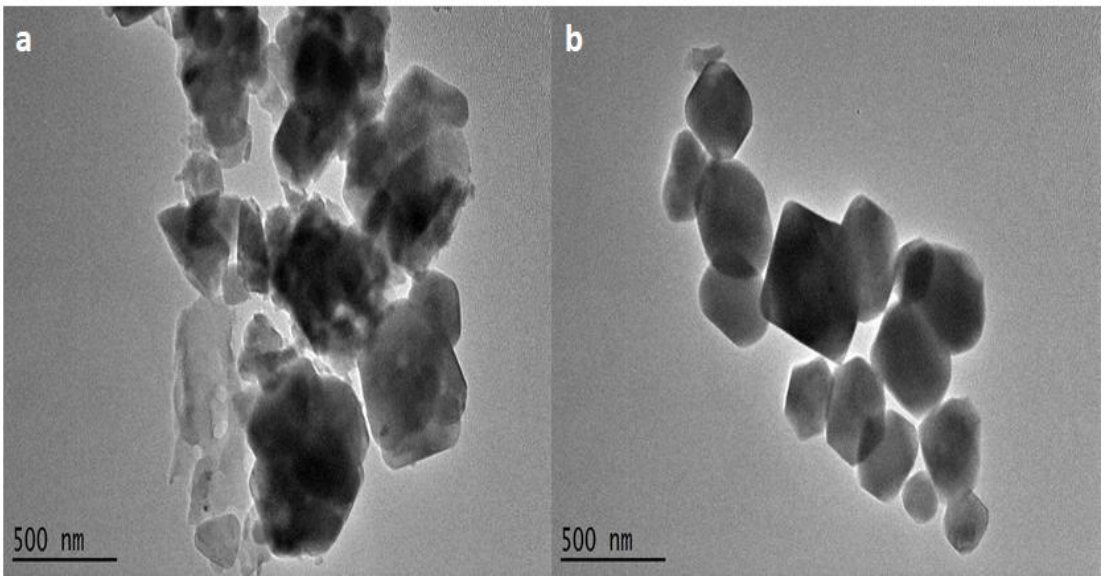

Figure 3. TEM images of (a) the nonporous SnP_2O_7 and (b) the meso-SnP_2O_7 samples.

Fig. 4a presents the typical isotherms of the type IV nitrogen adsorption and desorption curve. The mesoporous SnP_2O_7 exhibited a hysteresis loop, which suggests the presence of a lot of tiny pores in the network wherein nitrogen has not condensed at the high experiment pressure [11, 17]. Pore size distribution usually adopts the BJH (Barrett-Joiner-Halenda) model.

$In(p/P_0)=2\lambda V_m/r_mRT$ (Kelvein equation) (1)

Where λ,V_m and r_m are the adsorption of liquid surface tension, aperture radius and the adsorption of the liquid molar volume. Pore size distribution as shown in the inset. The inset exhibits a broad pore size distribution ranged from 1nm to 7 nm and a mean pore diameter of about ca. 4 nm for the mesoporous SnP_2O_7, which is in accordance with mesoporous in the IUPAC classification. Figure 4b mainly shows a pore size distribution and a mean pore diameter of ca. 75 nm for the nonporous SnP_2O_7.

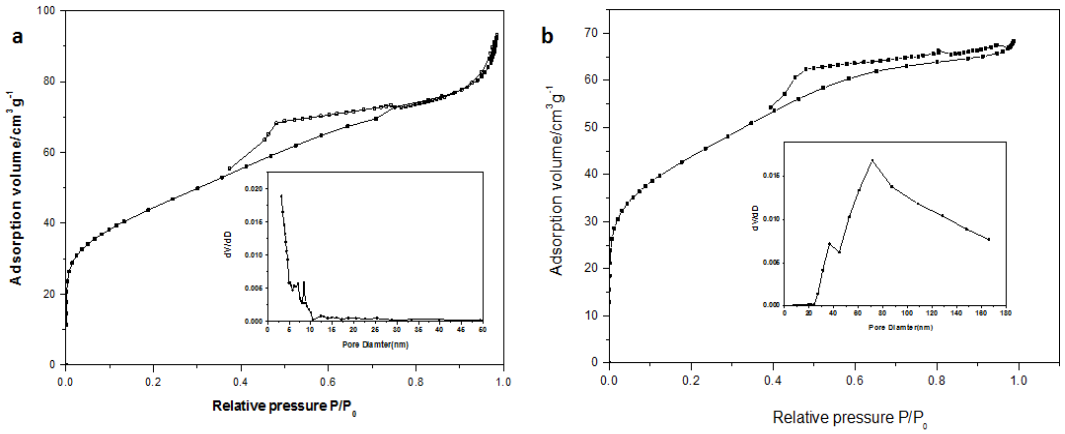

Figure 4. Nitrogen gas adsorption/desorption isotherm curves for (a) the meso-SnP_2O_7 and (b) nonporous SnP_2O_7 sample at 250 °C, the inset is the pore size distribution of the sample.

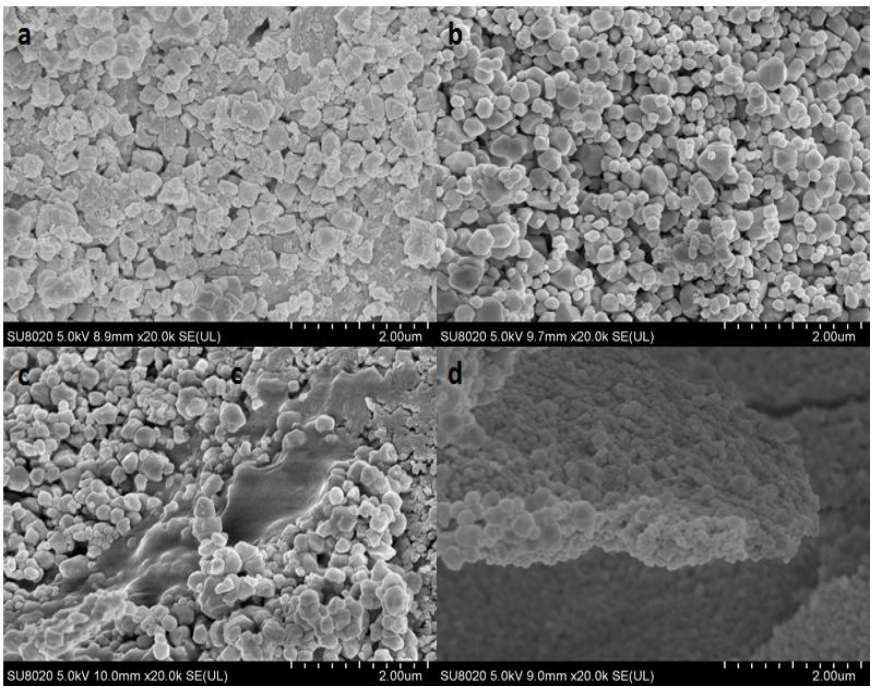

Figure 5. SEM images of membrane cross-sections: a) non-porous SnP_2O_7, b) Meso-SnP_2O_7, and c, d) Meso-SnP_2O_7/GO

Fig. 5 exhibits the morphology of the membrane cross-sections of non-porous SnP_2O_7, meso-SnP_2O_7, and meso-SnP_2O_7/GO. In Fig. 5a, the non-porous SnP_2O_7 particles are cubic phase in shape and mixed homogeneously. Fig. 5b depicts the mesoporous structure SnP_2O_7 appears square and hexagonal arrangement with smaller size, which may result in a compressed pores structure. As Fig 5c shown, GO is dispersed through the whole meso-SnP_2O_7/GO membrane. The GO sheets appear to remain exfoliated in the composite matrix and are already tightly fused in the inorganic material matrix. The meso-SnP_2O_7 particles are homogeneously dispersed and attached on the exfoliated layer GO as shown in Fig. 5d. Therefore, the conduction paths are established doping the GO throughout the whole membrane, and these conduction paths may explain the reason of high conductivity of the composite membrane. However, existing some pores are observed in the cross of pellet sample, which could be the gas transmit pathway that resulting in a crossover when fuel cell tests.

The thermal stabilities of the different structures SnP_2O_7 are shown in fig. 6. It is obvious that the non-porous SnP_2O_7 exhibits two clear degradation steps. The first step is attributed to the free water loss between 80°C and 120°C. The second step is the decomposition of cerium pyrophosphate into phosphate, metaphosphate and polyphosphate above 300 °C [18]. However, there is only a slight loss in weight from the meso-SnP_2O_7 sample from 25°C to 800 °C, indicating that the mesoporous structure materials are benefit in retention capability due to the capillary action and also the smaller size particles are much more stable in a high temperature range. The curve of meso-SnP_2O_7/GO exhibits a little more weight loss than that of meso-SnP_2O_7, that indicates a suitable aqueous retention capability of GO but a weak stability of the functional group.

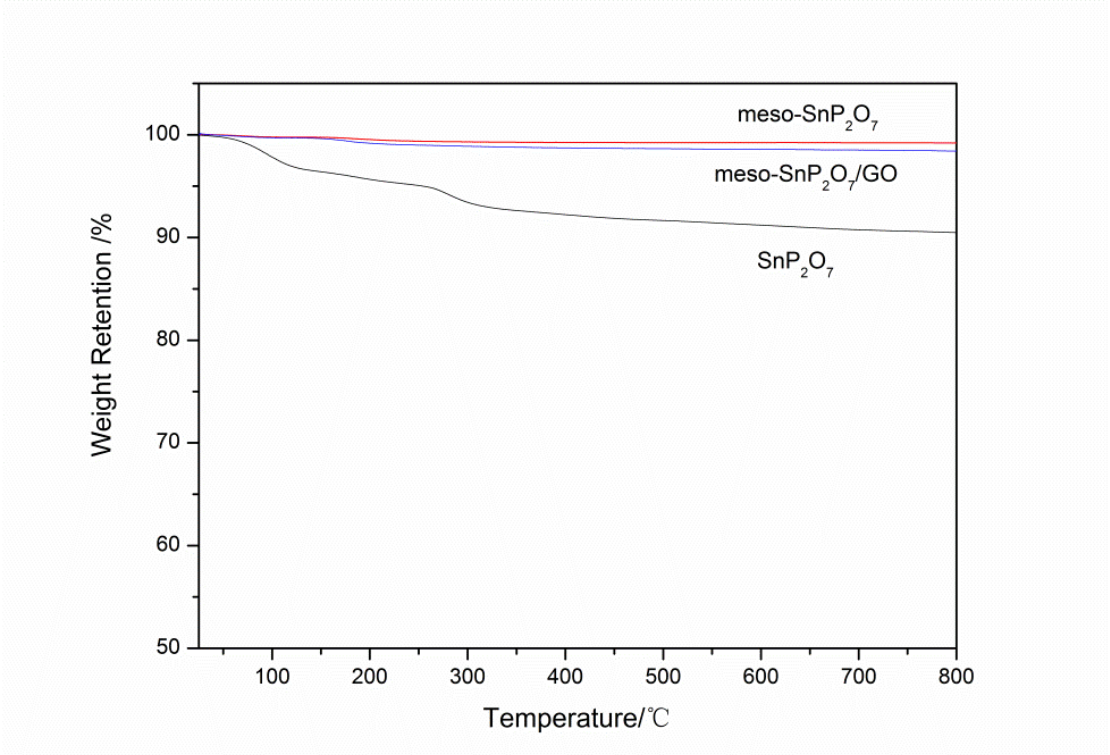

Figure 6. TGA of the non-porous SnP_2O_7, meso-SnP_2O_7, and meso-SnP_2O_7/GO heated from room temperature to 800 °C.

The conductivities of the membranes are calculated from the impedance data from 180°C to 280°C shown in fig. 7. The proton conductivity of the mesoporous SnP_2O_7 was around one order of magnitude higher than that of the nonporous SnP_2O_7 ranging from 180°C to 280°C. This is explained by assuming that the proton conductivity is mainly enhanced by the presence of proton ions dissolved in water molecules filled in the mesopores in favour of proton transport [11, 23-25]. The mesoporous SnP_2O_7 exhibits an increasing conductivity from 0.0091 S cm^{-1} to 0.015 S cm^{-1} in the temperatures range of 180-220 °C in Fig. 7. However, there is an obvious reduction in the conductivity when the temperature increases over 220°C, which could be attributed to the water lost from the capillary pores. It is obviously that the conductivity decrease of meso-SnP_2O_7 is much larger than that of non-porous SnP_2O_7. This result is good agreement of the literature work that the RH dependence was much larger for the mesoporous sample compared with the nonporous sample [11]. In the capillary-condensed water molecules, the proton concentration would be increased by the formation of hydroxyl groups from the incorporated protons. Moreover, the proton mobility would also be enhanced through the effective transport pathways along the highly hydrophilic pore walls.

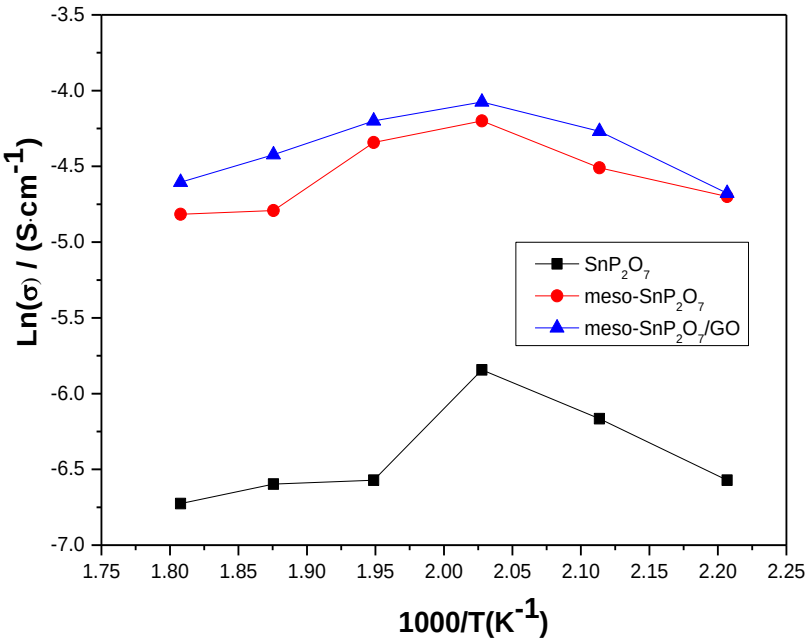

Figure 7. The conductivities of SnP_2O_7 and meso-SnP_2O_7 and meso-SnP_2O_7/GO composite electrolyte under anhydrous conditions

The Arrhenius plots for non-porous SnP_2O_7 and meso-SnP_2O_7 membranes are illustrated in Fig. 8. The conductivity follows the Arrhenius law [19, 20]:

$$\sigma = \sigma_0 exp\left(\frac{-E_a}{RT}\right) = \frac{A}{T} exp\left(\frac{-E_a}{RT}\right) \quad (2)$$

Where σ_0 and A are pre-exponential factors and Ea is the activation energy. The conductivity has been assumed that the phosphate deficiency caused a partial disconnection of the P_2O_7 network for proton conduction which follows the proton jump mechanism (Grotthuss mechanism) [21, 22]. Ion transport activation energies (Ea) of membranes obtained by the Arrhenius equation indicated the

barrier of charge carriers are decoupled from the sites movement [21, 22]. As shown in table 1, the activation energy of the meso-SnP_2O_7 membrane is 25.6 kJ mol^{-1}, which is obviously lower than the activation energy of meso-SnP_2O_7 (33.8 kJ mol^{-1}), resulting in a large energy barrier for proton jumps between sites and indicating the synergetic effect of capillarity. The activation energy of meso-SnP_2O_7 membrane is 20.8 kJ mol^{-1}, which is the lowest among the three materials. The lower activation energy requirement of the membrane indicated the proton conducting was easier to start.

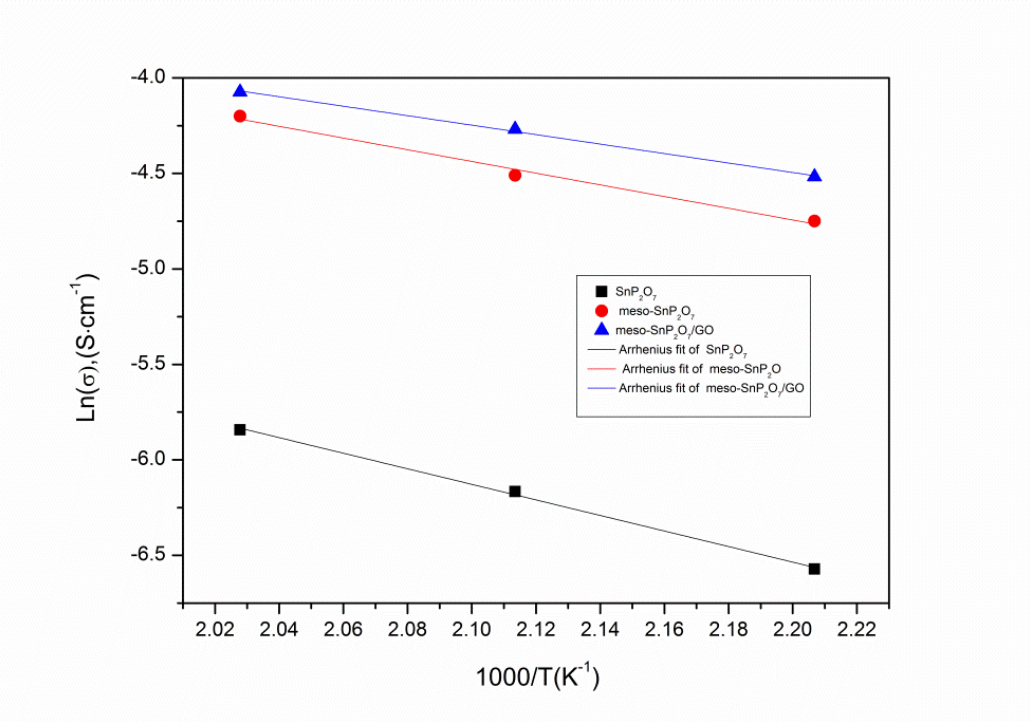

Figure 8. Arrhenius plots of non-porous SnP_2O_7 and Meso-SnP_2O_7 electrolyte

Table 1. Activation energy and conductivity of the membrane at 220°C

Membrane sample	Conductivity (S cm^{-1})	Ea (kJ mol^{-1})
Non-porous SnP_2O_7	0.0029	33.8
Meso-SnP_2O_7	0.015	25.6
Meso-SnP_2O_7/GO	0.017	20.8

The meso-SnP_2O_7/GO in Fig. 7 clearly illustrates a superior conductivity contrast to the meso-SnP_2O_7 membranes at different test temperatures. The maximum conductivity of meso-SnP_2O_7/GO is 0.017 S cm^{-2} at 220 °C. These results indicate that the GO filler in the composite membrane could provide efficient pathways for proton transmission leading to a faster proton transfer, because the hydrogen bonds in GO which exist acidic functional groups like carboxylic acid, epoxy oxygen could offer more facile hopping of protons to enhance the conductivity[12, 26]. GO also has a good water retention capability which benefit to the capillary condensation to fill the water in the mesopores [27, 28]. Therefore, the GO used in the inorganic composite membrane would be a suitable way to effectively improve the conductivity.

The fuel cell performances are obtained at 200°C and 220°C under anhydrous conditions for meso-SnP_2O_7 and meso-SnP_2O_7/GO are depicted in Fig. 9. The open circuit voltages (OCVs) of the SnP_2O_7 membranes are around 0.65V indicating a gas crossover which may be caused by the pores through the whole inorganic materials pellet which also observed in SEM image [29]. The OCV of meso-SnP_2O_7 is 0.73 V nearly 0.1V over the non-porous SnP_2O_7, because the smaller pore size of mesoporous structure and water molecule remain in the mesopores benefit to inhibit the gas crossover [11, 30, 31]. The OCV of the meso-SnP_2O_7/GO membrane (0.83 V) is further higher than that of the meso-SnP_2O_7 (0.73V) at 220°C. This result could be attributed to the exfoliated shape of the GO, which is tightly combined the powders together to hinder the gas transmit [27].

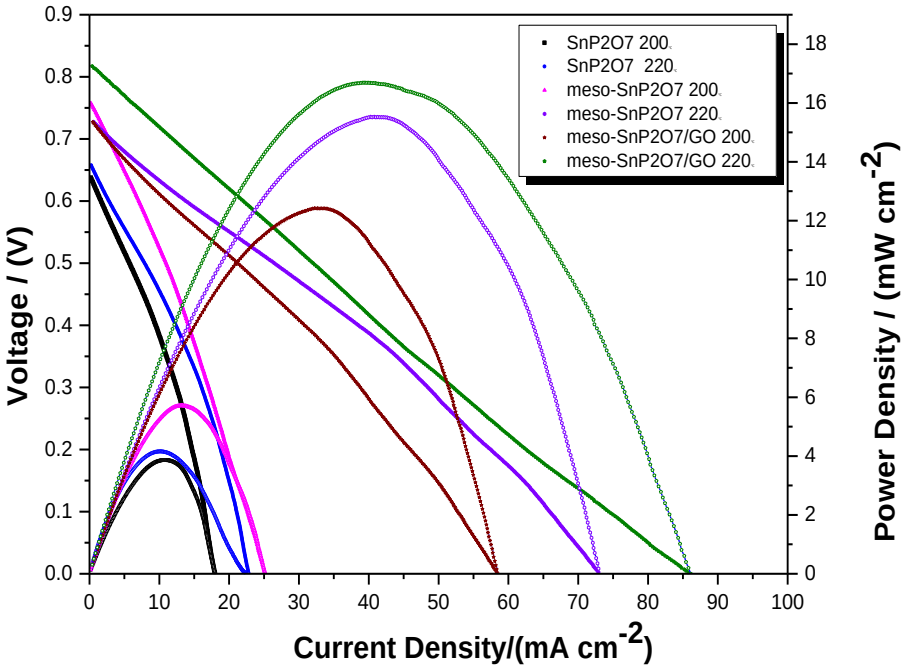

Figure 9. Polarisation and power density curves of fuel cells operated at 200 °C and 220 °C with 5 vol% H_2/Ar and air at atmospheric pressure.

GO incorporated with meso-SnP_2O_7 is an ideal way to overcome the gas crossover problem of the traditional tetravalent metal ions pyrophosphate electrolyte. Furthermore, the peak power density 17 mW cm^{-2} of meso-SnP_2O_7/GO contrasts with 15 mW cm^{-2} of meso-SnP_2O_7 at 220°C. This improved performance is mainly caused by the superior proton conductivity and OCV when the addition of GO [2, 27]. The acidic functional groups in GO, could provide more facile hopping of protons and enhance the conductivity through the more hydrogen bond formation [26]. The fuel cell performance improves as the temperature increases; the resultant peak power density of meso-SnP_2O_7/GO elevates from 12 to 17 mW cm^{-2} by increasing the temperature from 200 to 220°C. However, up to 240°C, the fuel cell performance decreases to 9 mW cm^{-2} (not shown in figure). This may be attributed to the excess the excess H_2O vapor present in the pores of the mesoporous inorganic produces transport pathways for protons followed the Grotthuss mechanism. Also in the capillary-condensed water molecules, the

proton concentration would be increased by the formation of hydroxyl groups from the incorporated protons leading to a higher proton mobility along the highly hydrophilic pore walls when the GO added [11, 31]. The results also correlate with the variation tendency of the membrane conductivities. The internal resistance values are estimated from the voltage losses. The voltage losses of the meso-SnP_2O_7/GO membrane-based fuel cell are 0.55 V and 0.29 V (from 0.02 to 0.05A cm^{-2}) at 220°C, and the resulting cell conductivities are approximately 0.0011 S cm^{-1}, which is similar to the conductivity test value. Therefore, the meso-SnP_2O_7/GO material is a potential candidate material for high temperature fuel cells at 200-240 °C.

4. CONCLUSIONS

Mesoporous SnP_2O_7 compounds were successfully synthesized through a phosphorylation reaction of mesoporous SnO_2. The mean particles and pore diameters of Meso-SnP_2O_7 were ca. 255 nm and 4 nm, respectively. The mesostructure makes high-temperature adsorption of aqueous vapour by capillary condensation which benefited to enhance the proton conductivity under low RH. The ion transport activation energies calculated from the Arrhenius law are explained by the Grotthuss mechanism in the capillary-condensed water molecules. The proton conductivity of meso-SnP_2O_7 reached 0.015 S cm^{-1} at 220 °C, which was nearly five times higher than that of non-porous SnP_2O_7. GO-incorporated mesoporous SnO_2 composite membranes exhibited an enhanced conductivity of 0.017 S cm^{-1} at 220°C, although the membrane conductivity subsequently decreased to 0.015 S cm^{-1} up to 240°C. The meso-SnP_2O_7/GO membrane provided superior fuel cell performance results (with a peak power density: 18 mW cm^{-2} at 220°C) which 50% higher than that of meso-SnP_2O_7 membrane (12 mW cm^{-2}). The GO incorporation with inorganic proton conductor exhibited improved conductivity and fuel cell performance, especially the OCV, indicating that meso-SnP_2O_7/GO could meet the requirement for practical high-temperature PEMFCs applications.

ACKNOWLEDGMENTS

The authors thank the funding support provided by the National Natural Science Foundation of China (21606064) and the Anhui Provincial Natural Science Foundation (1508085QB45). This project was also supported by The Project Sponsored by the Scientific Research Foundation for the Returned Overseas Chinese Scholars, State Education Ministry (JZ2015JYLH0084) and the 56th China Postdoctoral Science Foundation funded project and the Fundamental Research Funds for the Central Universities (2014HGQC0004).

References

1. Q. Li, R. He, J. Jensen, N. Bjerrum, *Fuel Cells*, 4 (2004) 147.
2. X. Huang, Y. Deng, C. Xu, L. Yang, Y. Hu, P. Luo, Y. Lu, J. Cheng, *Fuel*, 179 (2016) 299.
3. Y. Sato, Y. Shen, M. Nishida, W. Kanematsu, T. Hibino, *J. Mater. Chem.*, 22 (2012) 3973.
4. S. Authayanun, M. Mamlouk, A. Arpornwichanop, *Int. J. Hydrogen Energy*, 37 (2012) 6808.
5. B. Singh, H. Im, J. Park, S. Song, *J. Phys. Chem. C*, 117 (2013) 2653.

6. V. Nalini, M. Sorby, K. Amezawa, R. Haugsrud, H. Fjellvag, T. Norby, *J. Am. Ceram. Soc.*, 94 (2011) 1514.
7. A. Tomita, N. Kajiyama, T. Kamiya, M. Nagao, T. Hibino, *J Electrochem. Soc.*, 154 (2007) B1265.
8. Y.C. Jin, M. Nishida, W. Kanematsu, T. Hibino, *J. Power Sources*, 196 (2011) 6042.
9. B. Singh, H. Im, J. Park, S. Song, *J. Electrochem. Soc*., 159 (2012) 819.
10. P. Heo, K. Ito, A. Tomita and T. Hibino, *Angew. Chem., Int. Ed*., 47 (2008) 7841.
11. T. Hibino, K. Kabayashi, S. Fujit, *J. Mater. Chem*. A, 1 (2013) 13082.
12. C. Xu, Y. Cao, R. Kumar, X. Wu, X. Wang, K. Scott, *J. Mater. Chem*., 21 (2011) 11359.
13. D. Cai, M. Song, C. Xu, *Adv. Mater*., 20 (2008) 1706.
14. H. Zarrin, D. Higgins, Y. Jun, Z. Chen, M. Fowler, *J. Phys. Chem.* C, 115 (2011) 20774.
15. T. Hyodo, S. Abe, Y. Shimizu and M. Egashira, *Sens. Actuators* B, 93 (2003) 590.
16. H. Wang, J. Chen, R. Qiao, *Ceram. Int.*, 40 (2014) 8465.
17. M. Kruk and M. Jaroniec, *Chem. Mater*., 13 (2001) 3169.
18. M. Mamlouk, K. Scott, *J. Power Sources*, 286 (2015) 290.
19. R. He, Q. Li, G. Xiao, N. Bjerrum, *J. Mem. Sci*., 226 (2003) 169.
20. M. Li, K. Scott, X. Wu, *J. Power Sources*, 194 (2009) 811.
21. Y. Ma, J. Wainright, M. Litt, R. Savinell, *J. Electrochem. Soc*., 151 (2004) 8.
22. O. Paschos, J. Kunze, U. Stimming, F. Maglia, *J Phys. Condens. Matter*., 23 (2011) 234110.
23. M. Yamada, D. Li, I. Honma, H. Zhou, *J. Am. Chem. Soc*., 127 (2005) 13092.
24. M. Nogami, Y. Goto, Y. Tsurita and T. Kasuga, *J. Am. Ceram. Soc*., 84 (2001) 2553.
25. M. Nagao, T. Kamiya, P. Heo, A. Tomita, T. Hibino, M. Sano, *J Electrochem Soc*., 153 (2006) A1604.
26. C. Xu, X. Liu, J. Cheng, K. Scott, *J. Power Sources*, 274 (2015) 922-927
27. M. Huang, X. Huang, Y. Deng, M. Fei, C. Xu, J. Cheng, *Int. J. Hydrogen Energy*, 42 (2017) 1113.
28. V. Ponomareva, E. Shutova, *Solid State Ion.*, 178 (2007) 729.
29. T. Hibino, K. Kobayashi, *J. Mater. Chem. A*, 1 (2013) 6934
30. Y. Jin, Y. Shen and T. Hibino, *J. Mater. Chem.*, 20 (2010) 6214
31. Y. Zhou, J. Yang, H. Su, J. Zeng, S. Jiang, and W. Goddard, *J. Am. Chem. Soc.*, 136 (2014) 4954.